

X-ray Doppler Imaging of 44 ι Boo with *Chandra*

N. S. Brickhouse, A. K. Dupree, and P. R. Young

Harvard-Smithsonian Center for Astrophysics, 60 Garden Street, Cambridge, MA 02138

nbrickhouse@cfa.harvard.edu, adupree@cfa.harvard.edu, pyoung@cfa.harvard.edu

ABSTRACT

Chandra High-Energy Transmission Grating observations of the bright eclipsing contact binary 44 ι Boo show X-ray line profiles which are Doppler-shifted by orbital motions. The X-ray emission spectrum contains a multitude of lines superimposed on a weak continuum, with strong lines of O VIII, Ne X, Fe XVII, and Mg XII. The profiles of these lines from the total observed spectrum show Doppler-broadened widths of ~ 550 km s $^{-1}$. Line centroids vary with orbital phase, indicating velocity changes of > 180 km s $^{-1}$. The first-order light curve shows significant variability, but no clear evidence for either primary or secondary eclipses. Flares are observed for all spectral ranges; additionally, the light curve constructed near the peak of the emission measure distribution ($T_e = 5$ to 8×10^6 K) shows quiescent variability as well as flares. The phase-dependences of line profiles and light curves together imply that at least half of the emission is localized at high latitude. A simple model with two regions on the primary star at relatively high latitude reproduces the observed line profile shifts and quiescent light curve. These first clear X-ray Doppler shifts of stellar coronal material illustrate the power of *Chandra*.

Subject headings: atomic processes — binaries: close — stars: activity — stars: individual (44 ι Boo) — stars: late-type — X-rays: stars

1. Introduction

We report the first “X-ray Doppler imaging” of a late-type binary system, made possible by the high spectral resolution and stable wavelength scale of the *Chandra* High-Energy Transmission Grating (HETG). Phase-dependent line profile measurements of the contact binary 44 ι Boo, together with temperature-selected light curves, provide powerful new diagnostic capability.

Optical Doppler imaging of rapidly rotating RS CVn systems has demonstrated coronal activity patterns distinctly different from those of the Sun, with relatively stable polar active regions co-existing with more transient equatorial active regions (e.g. Vogt et al. 1999; Donati & Collier Cameron 1997). While optical Doppler imaging has been applied to RS CVn systems for more than a decade, only recently have Doppler images of a contact binary been reported, for the highly variable VW Cep, showing the presence of large polar spots, as well as low latitude features (Hendry & Mochnacki 2000).

In X-rays, the spectral resolution has until now been inadequate for line profile analysis of late-type stars. Eclipse mapping from light curve analysis has been used to infer the sizes and locations of flares (e.g. on Algol, Schmitt & Favata 1999; and on VW Cep, Choi & Dotani 1998); however, it is generally difficult to disentangle variability due to flaring from the modulation produced by either rotation or eclipses. The *EUVE* Deep Survey light curve for 44 ι Boo over 19.6 epochs shows no eclipses, but reveals quiescent modulation at the 50% level, associated with the rotation of the primary star; furthermore, EUV density diagnostics from the *EUVE* spectrometers suggest high density, implying localized coronal regions with small scale size $l \sim .004R_\star$, which must be located at high latitude (Brickhouse & Dupree 1998; hereafter, BD98). Determining the sizes and locations of coronal structures on contact binaries is an important step toward understanding the rotation/activity correlation, given that contact binaries are anomalously underluminous in X-rays, presenting normalized X-ray

fluxes (L_x/L_{bol}) 4 – 5 times weaker than those of the fastest rotating single stars (Stępien, Schmitt, & Voges 2001).

2. Observations

44ι Boo (HD 133640) is a triple star system containing a contact binary of the W UMa type, located a distance of 12.76 pc (ESA 1998). X-ray emission, first observed by Crudee & Dupree (1984), is expected to originate with the contact binary components B and C of the system. These two stars, of type G0 Vn (Gray, Napier, & Winkler 2001), orbit with a period of 6.4 hours and an inclination of 72.8° (Hill, Fisher, & Holmgren 1989).

Time-tagged HETG spectra of 44ι Boo, using the Advanced CCD Imaging Spectrometer-S (ACIS-S) detector, were obtained by *Chandra* on 2000 April 25 (ObsID 14). The system was observed for 59142 s, continuously covering 2.56 epochs of the orbit. The event lists were obtained from the Chandra X-ray Observatory Center (CXC) public archive as Level 1 files, and were then processed, using CXC software CIAO V2.1 and calibration database CALDB V5.0. High-Energy Grating (HEG) and Medium-Energy Grating (MEG) spectra were extracted as described by Canizares et al. (2001), and source-specific effective area curves were generated. Positive and negative first-order spectra were co-added.

3. Data Analysis

Here we link phase-dependent changes in the line profiles to the phase-binned behavior of the light curve, by applying the techniques of both eclipse mapping and X-ray Doppler imaging. Emission lines from the available Fe ionization stages provide broad coverage of electron temperature T_e and allow construction of a continuous emission measure distribution (EMD) model. The model EMD allows us to determine the T_e range contributing to the

emission lines of interest for profile analysis, as well as to predict which other spectral features arise from the same T_e range. Photons from all of these features are then selected from the event list to construct a new light curve characteristic of the line-emitting T_e .

3.1. Total Spectrum and Emission Measure Distribution

The total first-order spectrum of 44 ι Boo shows strong lines of H-like and He-like O, Ne, Mg, and Si, along with Fe L-shell lines from several ionization states. A weak continuum is also apparent. Table 1 gives the measured line fluxes and linewidths for the four strongest emission lines (O VIII, Ne X, and Mg XII Ly α and Fe XVII $2p^53d^1P_1-2p^61S_0$), as determined from Gaussian fits to the continuum-subtracted line profiles using the *Sherpa* package in CIAO. Line profiles are wider than the instrumental FWHM (240 and 460 km s $^{-1}$ at 15 Å, for HEG and MEG, respectively), with widths of ~ 550 km s $^{-1}$ corresponding to the spread of velocities in the system.

Strong, isolated Fe lines are used to construct the EMD: Fe XVII $\lambda\lambda 16.780; 17.051$; 17.096, Fe XVIII $\lambda\lambda 14.208; 15.625$, Fe XIX $\lambda 14.664$, Fe XXII $\lambda 11.770$, and Fe XXIII $\lambda 11.736$. The method is described by BD98 and we use the spectral models from the Astrophysical Plasma Emission Code (APEC; Smith et al. 2001). The EMD is characterized by a narrow peak at 8×10^6 K, similar to that found by BD98, but with the peak emission measure about 20% lower and the emission measure for $T_e > 10^7$ K about 50% higher.

Although the four strongest lines potentially represent a broad range of T_e , as characterized by their temperature of maximum emissivity T_{max} (see Table 1), in the 44 ι Boo spectrum they are all formed within a much narrower range. The EMD bump over the T_e range, $T_L = 5$ to 8×10^6 K, produces more than half of the flux for each of these lines (65, 83, 92, and 68%, respectively, for O VIII, Ne X, Fe XVII, and Mg XII). Models show that

the spectral region between 14 and 20 Å is primarily composed of line emission produced at T_L , and thus photons from this spectral region are used to construct the T_L light curve.

3.2. Light Curves

Figure 1 shows the optical light curve of Gheregá et al. (1994), which has subsequently been confirmed by eclipse timing measurements (Pribulla, Chochol, & Parimucha 1999; Albayrak & Gurol 2001). Primary eclipse (phase 0.00) corresponds to the eclipse of the secondary by the primary. Also shown are the *Chandra* total first-order light curve and the T_L light curve, limited to photons falling between 14 and 20 Å. The total light curve shows significant variability, but no clear evidence for either primary or secondary eclipses. A light curve constructed for high energy photons ($\lambda < 8$ Å; not shown) tracks the features of the total light curve, suggesting that the largest variations in total count rate are produced at the highest temperatures in the corona. The T_L light curve shows a different pattern of variability.

Four flares are identified in the total light curve, with the largest flare producing a peak count rate 3 times higher than the total count rate minimum. The T_L light curve shows three of the flares, with the largest flare producing only twice the count rate at peak compared to the T_L count rate minimum.

Excluding the times of obvious flares, the T_L light curve is notable in several respects which may reflect its “quiescent” behavior: (1) The T_L light curve is variable at the $\sim 20\%$ level, consistent with the X-ray variability found with *ROSAT* (McGale, Pye, & Hodgkin 1996). (2) Narrow dips occur immediately following each of the three primary eclipses, with remarkably similar shapes on each occurrence (Fig. 1). These dips indicate that emission is being absorbed, eclipsed, or rotated out of view. (3) A somewhat broader dip is observed

near one of the two secondary eclipses that occur during the *Chandra* pointing. This dip may also indicate occultation or a region rotating out of view; however, such an interpretation is not well supported because the other secondary eclipse coincides with a flare, observed in the total light curve, but not in the T_L light curve. Perhaps a dip effectively masks the T_L flare. (4) Excluding flares and dips, the T_L light curve is consistent with the *EUVE* finding (BD98) of sinusoidal variation with only one maximum, rather than two maxima as found in the optical light curve. Periodicity at or near the optical period, as found in the 19.6 epoch long *EUVE* observation, is not confirmed.

3.3. Phase-binned Line Profiles

Figure 2 shows the Ne X and Fe XVII line profiles summed over four equal phase intervals centered at Phase 0.00, 0.25, 0.50, and 0.75. Also shown are instrumental line profiles, centered at the laboratory wavelengths. While the MEG profiles have greater signal-to-noise, the factor of two greater resolving power of HEG allows much better isolation of different velocity components. The O VIII and Mg XII profiles (not shown) are similar, but with lower spectral resolution (HEG does not cover the O VIII line) or signal-to-noise ratio.

The rest wavelengths of these lines are well known. The H-like Ly α wavelengths are taken as the weighted average of the doublet, assuming they are optically thin and collisionally excited; the Fe XVII wavelength is $15.014 \pm .001$ Å (Brown et al. 1998). The absolute wavelength scale of the HETG is currently only accurate to about 100 km s^{-1} ; however, the scale appears to be very stable, such that *relative* wavelength measurements are secure to better than 100 parts per million, or about 30 km s^{-1} (CXC Proposers’ Observatory Guide 2001). The reality of individual features in the line profiles is more difficult to assess, but we expect that significant deviations from a Gaussian profile, occurring over several bins, reflect real features. The profiles contain multiple components representing a range of velocities.

Roughly one third of the emission is always present within the instrumental line profile, and cannot be resolved. Excluding data during the flare times (Fig. 1) does not affect these components.

Median wavelengths are determined from MEG line profiles as the interpolated center of the count distribution, with Poisson errors assumed. Continuum and weaker background are not subtracted, as they appear to contribute at most 20 counts to any of the total integrated MEG lines. Figure 3 shows the shift of the median wavelengths for each line, for the same four orbital phase bins as in Figure 2. Centroids determined from separate MEG and HEG fits to Gaussian line profiles are consistent with these medians, but give larger errors where the profiles appear distinctly non-Gaussian. The four ions studied show similar patterns of velocity shifts as a function of orbital phase. Relative velocity changes with phase exceed the instrumental uncertainties, and suggest net velocity changes of 180 km s^{-1} over the orbit. Ne X has sufficient counts to verify that the patterns of line shifts repeat from one epoch to the next.

4. Modeling the Coronal Activity

We present a simple 2-component model of the variability due to quiescent coronal structures. The lack of eclipse signatures (two maxima and two minima per orbit) severely limits the amount of emitting material that can be evenly distributed near the surfaces of both stars, since the equatorial regions would then be eclipsed. Diffuse extended emission is also strictly limited, since the integrated broad line profiles show distinct velocity components which change with phase. The T_L light curve shows about 20% quiescent modulation, implying that most of the material is always visible, i.e. located at high latitude. Flares are not correlated with phase, consistent with the active regions being visible most of the time.

Our model attempts to match the observed features: (a) phase-dependent line shifts; (b) broad sinusoidal T_L light curve modulation found from *EUVE* (BD98) and confirmed with the present observation; and (c) narrow dips in the T_L light curve. Two regions contribute roughly equally to the total emission in order to account for similar drops in the count rate during the narrow dips and broad minima. Since line centroids show velocity shifts consistent with the motion of the primary star, we place both active regions on the primary star. They are assumed to lie on the star's surface. The distinctive dip in the light curve just after phase 0.0 can only be explained as a small emitting region R1 on the inner face of the primary, which briefly rotates out of view. R1 must extend below a latitude of 72.8° in order to be occulted, but not extend below $\approx 70^\circ$ so that the dip remains narrow. (Of course, if the material is extended above the stellar surface, the latitude constraint is weakened.) For the same reason R1 cannot extend more than $\approx 10^\circ$ in longitude.

To reproduce the broader modulation requires a larger region R2 on the outer face of the primary in order to yield a light curve maximum at phase ≈ 0.2 . R2 must also be at high latitude in order to produce the weak $\sim 20\%$ modulation. Figure 4 shows that the light curve produced from a particular choice of the regions R1 and R2 mimics the key features of the *Chandra* T_L light curve. Simulations of the system with different active region locations and sizes, including radially extended regions, are underway to study the effects on light curves and line profiles.

5. Conclusions

The *Chandra* observations of 44 ι Boo provide the first clear evidence from line profile velocity measurements for localized activity at high latitude on the primary star. Our interpretation is supported by the phase-dependent light curves for emission produced at the temperature of the EMD bump. Location of activity on the primary star has been consid-

ered in the past to explain peculiarities and changes in the photometric behavior of W UMa binaries, although a strong theoretical basis for such a preference is lacking (Rucinski 1985). Coronal enhancements that we find associated with the primary provide added support for the dominance of the primary in magnetic activity as other studies have indicated (BD98; Choi & Dotani 1998; Barden 1985). These results demonstrate the power of *Chandra* for understanding coronal structure, using eclipse mapping and X-ray Doppler imaging.

This work was supported in part by NASA NAG5-3559 and the Chandra X-Ray Observatory Center NASA NAS8-39073 from NASA to the Smithsonian Astrophysical Observatory and by Johns Hopkins Contract #2480-60016.

REFERENCES

Albayrak, B., & Gurol, B. 2001, IBVS, No. 5069

Barden, S. C. 1985, ApJ, 295, 162

Brickhouse, N. S., & Dupree, A. K. 1998 (BD98), ApJ, 502, 918

Brown, G. V., Beiersdorfer, P., Liedahl, D. A., Widmann, K., & Kahn, S. M. 1998, ApJ, 502, 1015

Canizares, C. R., et al. 2001, ApJ, 539, L41

CXC Proposers Observatory Guide V.3 2001, (Cambridge: Chandra X-ray Observatory Center)

Choi, C. S., & Dotani, T. 1998, ApJ, 429, 761

Cruddace, R. G. & Dupree, A. K. 1984, ApJ, 177, 263

Donati, J.-F. et al. 1992, A&A, 265, 682

ESA, 1998, The Hipparcos Catalogue, ESA SP-1200 (Noordwijk: ESA)

Favata, F., & Schmitt, J. H. M. M. 1999, A&A, 350, 900

Ghorega, O., Farkas, L., & Horvath, A. 1994, IBVS, No. 4045

Gray, R. O., Napier, M. G., & Winkler, L. I. 2001, ApJ, 121, 2148

Hendry, P. D., & Mochnacki, S. W. 2000, ApJ, 531, 467

Hill, G., Fisher, W. A., & Holmgren, D. 1989, A&A, 211, 81

McGale, P. A., Pye, J. P., & Hodgkin, S. T. 1996, MNRAS, 280, 627

Pribulla, T., Chochol, D., & Parimucha, S. 1999, IBVS, No. 4751

Rucinski, S. M. 1985, in *Interacting Binaries*, ed. P. P. Eggleton & J. E. Pringle, (Boston: D. Riedel), 13

Schmitt, J. H. M. M., & Favata, F. 1999, Nature, 410, 44

Smith, R. K., Brickhouse, N. S., Raymond, J. C., & Liedahl, D. A. 2001, ApJ, 556, L91

Stępien, K., Schmitt, J. H. M. M., & Voges, W. 2001, A&A, 370, 157

Vogt, S. S., Hatzes, A. P., Misch, A. A., & Kurster, M. 1999, ApJSupp, 121, 547

Table 1. Strong Line Measurements

Ion	λ (Å)	MEG	HEG	Flux	MEG FWHM	HEG FWHM	T_{max}
		(Cnts)	(Cnts)	(ph cm ⁻² s ⁻¹)	(mÅ)	(mÅ)	(K)
O VIII	18.969	721	...	$1.21 \pm 0.05 \times 10^{-3}$	34.2 ± 1.4	...	3×10^6
Ne X ^a	12.134	1544	434	$5.18 \pm 0.14 \times 10^{-4}$	29.4 ± 0.1	23.4 ± 1.4	5×10^6
Fe XVII	15.014	401	121	$3.87 \pm 0.23 \times 10^{-4}$	33.2 ± 2.3	25.4 ± 3.6	5×10^6
Mg XII	8.421	347	163	$5.94 \pm 0.38 \times 10^{-5}$	23.7 ± 1.7	17.2 ± 2.0	8×10^6

^aThe contribution of Fe XVII λ 12.124 is estimated to be only $\sim 7\%$, based on ratios with Fe XVII λ 17.051.

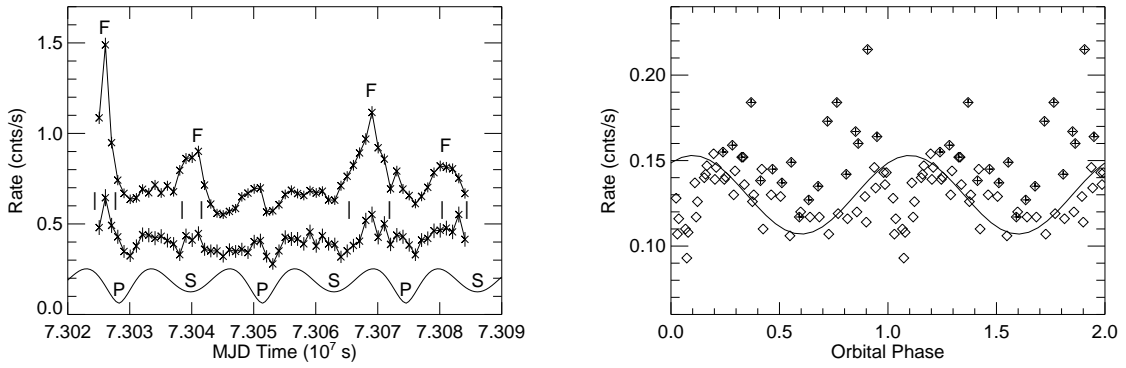


Fig. 1.— *Left*: Count rate vs MJD (s) for 1000 s time intervals. The uppermost curve is the total first-order light curve. The middle curve represents the low temperature T_L ($14 \text{ \AA} < \lambda < 20 \text{ \AA}$) light curve (count rate $\times 3$). The lowest curve is the scaled optical light curve, with the primary (P) and secondary (S) minima marked. Four flares (F) are identified, with vertical bars denoting their extent. *Right*: Count rate vs orbital phase for the same T_L light curve shown above. Data (\diamond) are phase-folded over two epochs. Plus symbols (+) are overplotted for the flare times marked with vertical bars on the figure above (*left*). A sine curve is overlaid on the light curve for illustration.

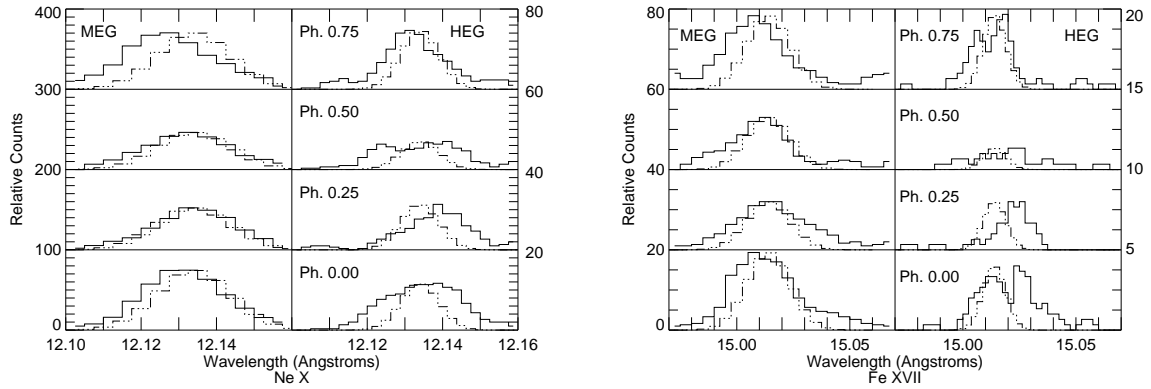


Fig. 2.— Ne X (*left*) and Fe XVII (*right*) MEG and HEG line profiles (solid) for each phase. Binsizes are 0.005 and 0.0025 Å, respectively, and spectra are box-car smoothed over 3 bins. The zero points of the spectra are shifted up for each phase, but the scales are the same. The exposure time is not the same for each phase bin, so integrated counts will differ. For each profile, the instrumental line profile (dash-dotted) is shown for comparison, with peak set to the data peak and centroid set at the laboratory wavelength.

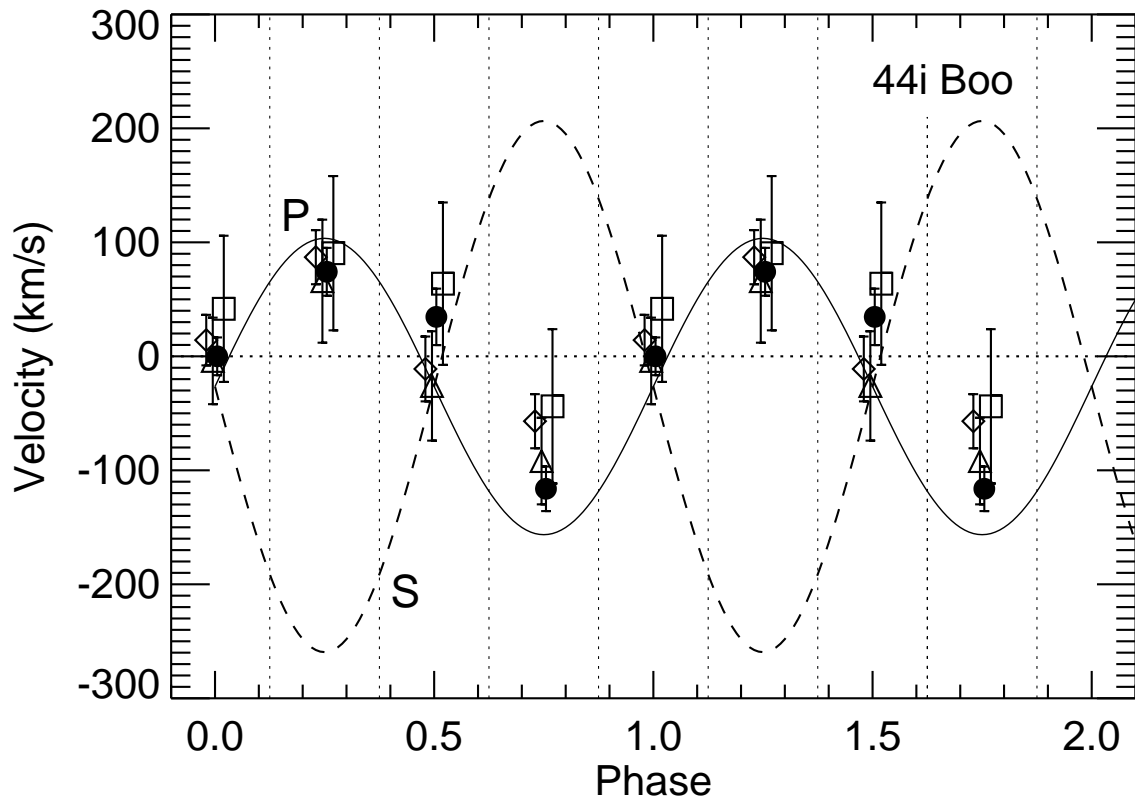


Fig. 3.— Velocities as a function of orbital phase, as measured from MEG profiles. Velocities are derived from the median centroid shifts for the phase bins indicated by vertical dashed lines. The four symbols represent O VIII (\diamond), Ne X (\bullet), Fe XVII (Δ), and Mg XII (\square). Error bars represent statistical errors only. The different symbols are shifted slightly from their phase centers for plotting. Radial velocity curves for the primary (solid) and secondary (dash-dotted) are from Hill et al. (1989).

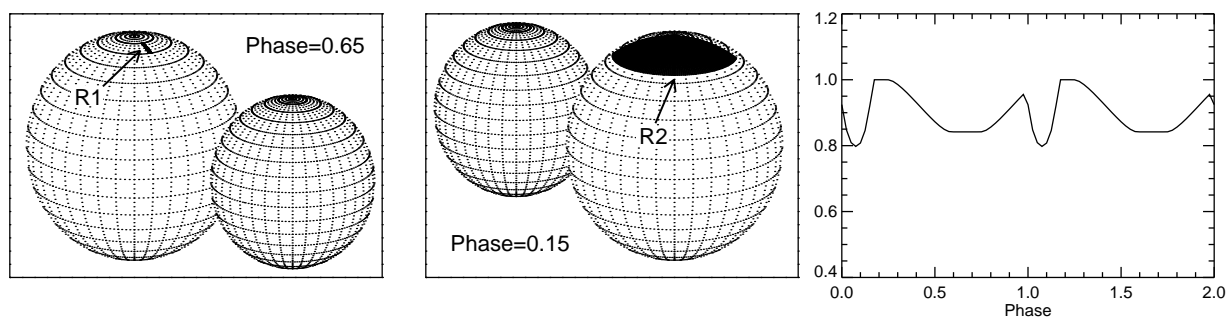


Fig. 4.— Simulation of two active regions R1 and R2, described in text, with model light curve.